Journal of Alloys and Compounds 855 (2021) 157317

Contents lists available at ScienceDirect

Journal of Alloys and Compounds

journal homepage: http://www.elsevier.com/locate/jalcom

Development of low-alloyed Mg–Zn–Ca–Sn–Mn alloy with high strength-ductility synergy by sub-rapid solidification and hot rolling

Zhen-Ming Hua [b, c], Bing-Yu Wang [b], Cheng Wang [b, **], Chen-Yi Ma [b], Pin-Kui Ma [b], Zhi-Ping Guan [b], Yi-Jia Li [b], Jia-Sheng Li [b], Hui-Yuan Wang [a, b, c, *]

[a] State Key Laboratory of Automotive Simulation and Control, Jilin University, Changchun, 130012, PR China
[b] Key Laboratory of Automobile Materials of Ministry of Education & School of Materials Science and Engineering, Nanling Campus, Jilin University, No. 5988 Renmin Street, Changchun, 130025, PR China
[c] International Center of Future Science, Jilin University, Changchun, 130012, PR China

ARTICLE INFO

Article history:
Received 8 April 2020
Received in revised form
5 September 2020
Accepted 22 September 2020
Available online 23 September 2020

Keywords:
Mg–Zn–Ca alloy
Sub-rapid solidification
Low alloying
Mechanical properties
Slip trace analysis

ABSTRACT

Achieving high strength-ductility synergy is a great challenge in low-alloyed Mg alloys. In this work, a new Mg–1.0Zn–0.45Ca–0.35Sn–0.2Mn (wt.%, ZXTM1000) alloy was designed and fabricated by sub-rapid solidification (SRS) to overcome the dilemma. After hot rolling and annealing, the new alloy sheet exhibited an excellent tensile yield strength (YS, ~270 MPa) and elongation (~21%). Microstructure characterization revealed that the high YS was mainly attributed to the fine grains (~3 μm) and high density of spherical $Ca_2Mg_6Zn_3$, Mg_2Ca, and α-Mn precipitates. Moreover, the homogeneous grain size distribution, weakened TD-split texture and the activation of multiple types of slips contributed to the enhanced ductility. The findings demonstrate an effective way to fabricate low-alloyed Mg alloys with high strength and ductility by combining the SRS and hot rolling.

1. Introduction

Magnesium (Mg) alloys have drawn crucial attention for its low density and high specific strength, but the expectant broad application is restricted by inferior yield strength (YS) and poor deformation ability [1]. Element alloying is brought forward as an effective method to address these problems [2,3]. For example, Sasaki et al. [4] developed an extruded Mg–6.6Sn–5.9Zn–2.0Al–0.2Mn (wt.%) alloy, exhibiting an excellent YS of 370 MPa with an elongation (EL) of 14%. Note that high content alloying is conducive to improving mechanical properties, while it also increases the cost and brings difficulties in the processing of alloys for industries [5,6]. A low-alloyed Mg alloy usually exhibits insufficient YS for industry applications unless the ductility is significantly sacrificed. Severe plastic deformation (SPD) is used to improve the strength and ductility simultaneously based on the grain refinement [7,8]. However, it is still a big challenge for industries to fabricate large-scale Mg alloy components by the SPD.

The dissatisfactory YS of low-alloyed Mg alloys originates from the grain coarsening during thermal-mechanical processes and the disappointing precipitation hardening [9]. Introducing a high volume fraction of nano-precipitates to the Mg matrix can not only inhibit grain growth but also trigger precipitation hardening. To increase the density of nano-precipitates, micro-alloying with multiple elements would be a promising strategy. The addition of Zn and Ca facilitates the formation of thermostable $Ca_2Mg_6Zn_3$ and Mg_2Ca phases, which is beneficial for grain refinement and aging hardening [2,10]. Moreover, the solid-solution of Zn and Ca atoms can also improve the formability by facilitating non-basal slips [11] and weakening basal texture [12]. Trace addition of Sn and Mn would be used to furtherly stabilize the microstructure due to the pinning effect from CaMgSn [2,13] and Mn [10,14] precipitates. Note that the Ca-containing eutectic phases, formed in the Mg–Zn–Ca–Sn series alloys during solidification, prefer to exist at dendrite boundaries [2,13]. These eutectic phases, which are brittle and typically coarse, tend to fracture and detach from the Mg matrix, and result in the pile-up of dislocations and hence high-stress localization, acting as crack sources during deformation. However, it is difficult to homogenize and dissolve the coarse eutectic Ca-containing phases into the Mg matrix, even at 500 °C for 24 h, which prevents alloying elements from fully exerting their strengthening and toughening potential [15,16].

* Corresponding author. International Center of Future Science, Jilin University, Changchun, 130012, PR China.
** Corresponding author.
E-mail addresses: chengwang@jlu.edu.cn (C. Wang), wanghuiyuan@jlu.edu.cn (H.-Y. Wang).

https://doi.org/10.1016/j.jallcom.2020.157317
0925-8388/

The cooling rate plays an important role in the evolution of as-cast microstructure. Note that the sub-rapid solidification (SRS), with a high cooling rate ranging from 10^2 to 10^3 K/s, can significantly refine the dendrites and eutectic phases, compared with the conventional solidification (CS) procedure (cooling rate < 10^2 K/s). The microstructure refinement is originated from the increased nucleation rate induced by larger undercooling and inhibited grain growth under the SRS [17–20]. Moreover, Xu et al. [17] and Wang et al. [21] demonstrated that the Mg–Al–Ca–Mn series alloys with a higher cooling rate (~100 K/s) during solidification exhibited finer grain size after extrusion, compared with the samples with lower cooling rate (~15 K/s), leading to an enhanced YS in the former case. Besides, the higher cooling rate during solidification would also lead to the reduced diffusion time of solutes, resulting in effective solute trapping in the Mg matrix, which is beneficial for precipitation during subsequent thermomechanical deformation [17]. Although rapid solidification (cooling rate > 10^3 K/s) could further modify the as-cast structure, the SRS is expected to be easily operated and scaled-up [18].

In this paper, a novel low-alloyed Mg–1.0Zn–0.45Ca–0.35Sn–0.2Mn (wt.%, ZXTM1000) alloy is fabricated based on the SRS, showing an good combination of strength and ductility after hot rolling and annealing. The systematic microstructure characterizations and the analysis of strengthening mechanisms illustrate the reasons for the high strength-ductility synergy in our developed alloy. Moreover, to demonstrate the significance of the utilization of SRS, the ZXTM1000 alloy is also prepared by CS and experiences the same thermomechanical processes for comparison.

2. Experimental procedures

The ZXTM1000 alloy was prepared from commercial pure Mg (99.90 wt%), pure Zn (99.90 wt%), pure Sn (99.90 wt%), Mg–25Ca (wt.%), and Mg–5Mn (wt.%) in an electric resistance furnace under the protection of a gas mixture of 99.5% CO_2 and 0.5% SF_6 at ~680 °C. After being purified and kept for about 15 min, the melts were poured into the water-chilled copper molds with cavity sizes of 80 mm (L) × 50 mm (W) × 20 mm (T), and 80 mm (L) × 50 mm (W) × 5 mm (T), where L stands for length, W stands for width, and T stands for thickness, denoted as the as-cast CS and SRS ZXTM1000 alloys, respectively. Rolling slabs with dimensions of 40 mm × 25 mm × 5 mm were cut from the as-cast samples and hot-rolled at 300 °C from ~5 mm to ~0.85 mm by 5 passes, with ~30% thickness reduction per pass, denoted as the rolled ZXTM1000 alloy. Before each rolling pass, the samples were preheated at 300 °C for 10 min. Finally, the rolled sheets were annealed at 300 °C for 15 min, denoted as the annealed ZXTM1000 alloys.

The K-type thermocouples and data acquisition hardware (EM9104C, ZTIC, China) were utilized to collect the real-time data of solidification temperature at a scanning frequency of 200 Hz. The microstructure was characterized by optical microscopy (OM), scanning electron microscopy (SEM), electron backscatter diffraction (EBSD), and transmission electron microscope (TEM, JEM-2100F, operating at an accelerating voltage of 200 kV). For EBSD characterization, the SEM (TESCAN, VEGA3 XMU, Czech) equipped with an Oxford Instruments NordlysNano EBSD detector was utilized for the annealed ZXTM1000 alloys, while an FE-SEM (Zeiss, Sigma 500) equipped with an Oxford Instruments Symmetry EBSD detector was adopted for the rolled and tension-deformed ZXTM1000 alloys. The tensile tests were carried out along the rolling direction (RD) using an AGS-X-100 kN electric universal testing machine coupled with a video extensometer under the strain rate of 1.0×10^{-3} s^{-1}. Dog-bone specimens with a gauge size of 10 mm × 4 mm × 0.8 mm were employed for the tensile tests by at least three times.

Metallographic specimens were conventionally ground, manually polished, and etched for about 15 s in an acetic picric solution (1.5 g picric acid, 2 mL acetic acid, 3 mL distilled water, and 25 mL ethyl alcohol). Before the EBSD characterization of the rolled samples, an annealing treatment at 250 °C for 10 min was employed to release the severe stress concentration caused by rolling to improve the index. The EBSD data were analyzed via the HKL CHANNEL5 software. For the clean-up procedure, the *Wild Spikes* were extrapolated firstly, and then a medium level of *Zero solution* extrapolation with the neighbour of 5 was performed. Moreover, the recrystallized grains were defined with the value of grain orientation spread (GOS) less than 1°, while the value of GOS for deformed grains was larger than 7.5°, and the grains with the value of GOS ranging from 1° to 7.5° were defined as substructured grains. Thin foil specimens for TEM observation were prepared through mechanical grinding to ~70 μm thickness followed by ion-beam thinning. The dislocation types of the annealed SRS ZXTM1000 specimen were observed under the two-beam diffraction conditions.

3. Results

3.1. Microstructure of the as-cast CS and SRS ZXTM1000 alloys

Fig. 1 shows the cooling curves of the as-cast CS and SRS ZXTM1000 alloys. The cooling rate of Mg melts was evaluated based on the interval between pouring temperature and solidification onset temperature (liquidus point) [22], which is the slope of the initial linear descent stage of the cooling curve. The cooling rates are ~20 K/s and ~200 K/s for the CS and SRS alloys, respectively.

Fig. 2a–d show the as-cast microstructure of the CS and SRS ZXTM1000 alloys. The SRS alloy has a significantly finer grain size of ~100 μm, compared with that of ~240 μm for the CS counterpart. Both of the alloys contain CaMgSn phase (indicated by red arrows) located at GBs and spherical $Ca_2Mg_6Zn_3$ phase (indicated by yellow arrows) distributed within grains, which is consistent with reference [2]. Note that the morphology of CaMgSn transforms from the lamellar shape (Fig. 2c) into the tadpole shape (Fig. 2d) along GBs when the cooling rate is increased from ~20 K/s to ~200 K/s. Distinctly, these brittle Ca-containing phases in the SRS alloy (Fig. 2d) exhibit more uniform distribution with a finer size than the CS counterpart (Fig. 2c).

3.2. Microstructure of the rolled and annealed CS and SRS ZXTM1000 alloys

After hot rolling, the microstructure of both alloys is remarkably refined, compared with the as-cast state. However, the grain size of the rolled SRS ZXTM1000 alloy (Fig. 3b) is still smaller than that of the rolled CS counterpart (Fig. 3a). Numerous low-angle grain boundaries are formed within the two alloys, and there are large accumulated misorientation angles in the deformed grains, e.g. ~0.8 deg/μm and ~3.3 deg/μm for the rolled CS and SRS alloys, respectively (Fig. 3c), which indicates that the continuous dynamic recrystallization (CDRX) process dominated during hot rolling [23]. Many double twin boundaries (DTWs, red lines) and contraction twin boundaries (CTWs, green lines) can be detected in the rolled CS (Fig. 3d) and SRS alloys (Fig. 3e), which are expected as the favorable sites for static recrystallization during subsequent annealing treatment [24].

Fig. 4a and b illustrate the microstructure evolution in the annealed CS and SRS ZXTM1000 alloys. The fragmental phases in the SRS alloy (Fig. 4b) are finer and distribute relatively more uniform along the RD than those in the CS alloy (Fig. 4a). The broken second phases in the CS alloy are concentrated in some regions (Fig. 4a), which would lead to the localized strain intensification

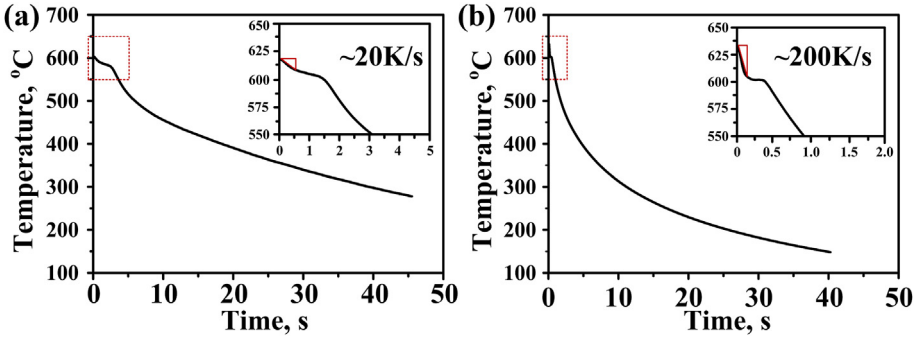

Fig. 1. Cooling curves of the as-cast (a) CS and (b) SRS ZXTM1000 alloys.

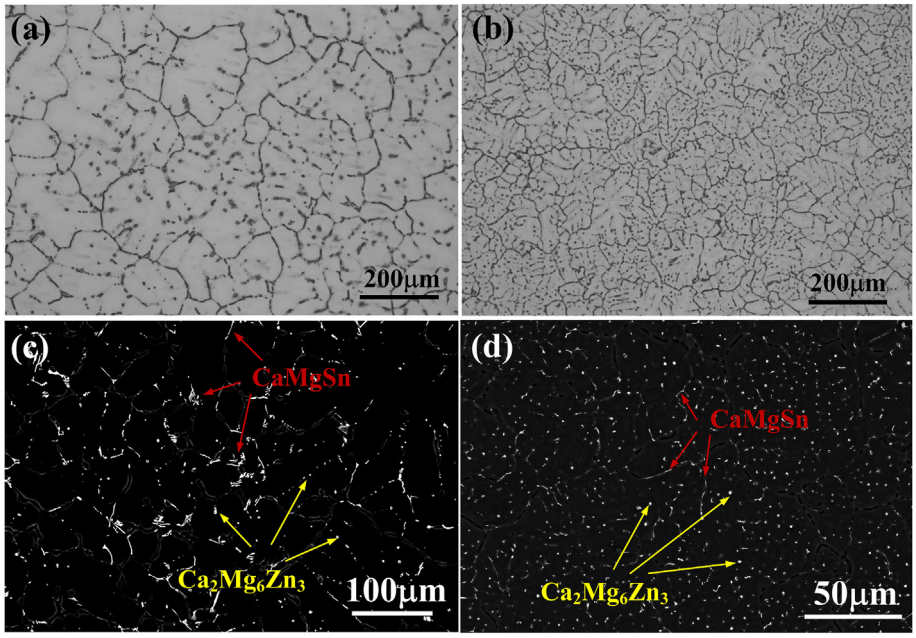

Fig. 2. (a, b) Optical and (c, d) SEM-BSE images of as-cast (a, c) CS and (b, d) SRS ZXTM1000 alloys.

and the generation of micro-cracks during tensile deformation, deteriorating the strength and ductility of the alloy [25].

Fig. 5a and d reveal that both CS and SRS ZXTM1000 alloys exhibit homogeneous fine-grained structure with modified basal texture after rolling and annealing, wherein the basal pole splits from the normal direction (ND) towards the transverse direction (TD), denoted as TD-split texture. Note that the annealed SRS ZXTM1000 alloy (Fig. 5d) shows a finer average grain size of ~3 μm, while that for the CS alloy (Fig. 5a) is ~5 μm, which is similar to the phenomenon in the as-cast and rolled samples. Apart from the grain size, the annealed CS ZXTM1000 alloy exhibits similar average SF_{basal} value involving tension along RD (Fig. 5b) and recrystallization fraction (Fig. 5c) to those of the annealed SRS alloy (Fig. 5e and f).

3.3. Mechanical properties of the annealed CS and SRS ZXTM1000 alloys

The tensile true stress-strain curves of the annealed CS and SRS ZXTM1000 alloys are shown in Fig. 6a. The SRS alloy exhibits a high YS of ~270 MPa, ultimate tensile strength (UTS) of ~305 MPa, and EL of ~21%, which are ~45 MPa, ~50 MPa and ~7% higher than those in the CS counterpart (Fig. 6b). The simultaneous improvement in strength and ductility of the SRS alloy results from its finer grain size and modified size and distribution of Ca-containing eutectic phases than those of the CS alloy.

Fig. 6c summarizes the YS as a function of elongation for various wrought Mg alloys with alloying content smaller than 4 wt%. The annealed SRS ZXTM1000 alloy developed in this work shows an excellent strength-ductility balance compared to previously studied Mg–Zn–Ca-based alloys and other commercially available Mg wrought alloys such as Mg–Al–Zn and Mg–Zn series. The relationship between the work-hardening rate ($d\sigma/d\varepsilon$) vs. true strain for the annealed SRS alloy is shown in Fig. 6d. After a brief increase, the work-hardening rate value witnesses a continuous decrease, implying that multiple slips are activated to accommodate deformation during tension. As shown in the present work and literature, the SRS exhibits overwhelming advantages over the CS in homogenizing and refining the microstructure. The following characterization would be focused on the annealed SRS ZXTM1000 alloy to explore the reasons for high strength-ductility synergy.

3.4. TEM analysis of the annealed SRS ZXTM1000 alloy

Bright-field (BF) TEM images (Fig. 7a and b) show that there are some sub-micron and numerous nano-sized spherical particles distributing at GBs, which plays an effective role in inducing the

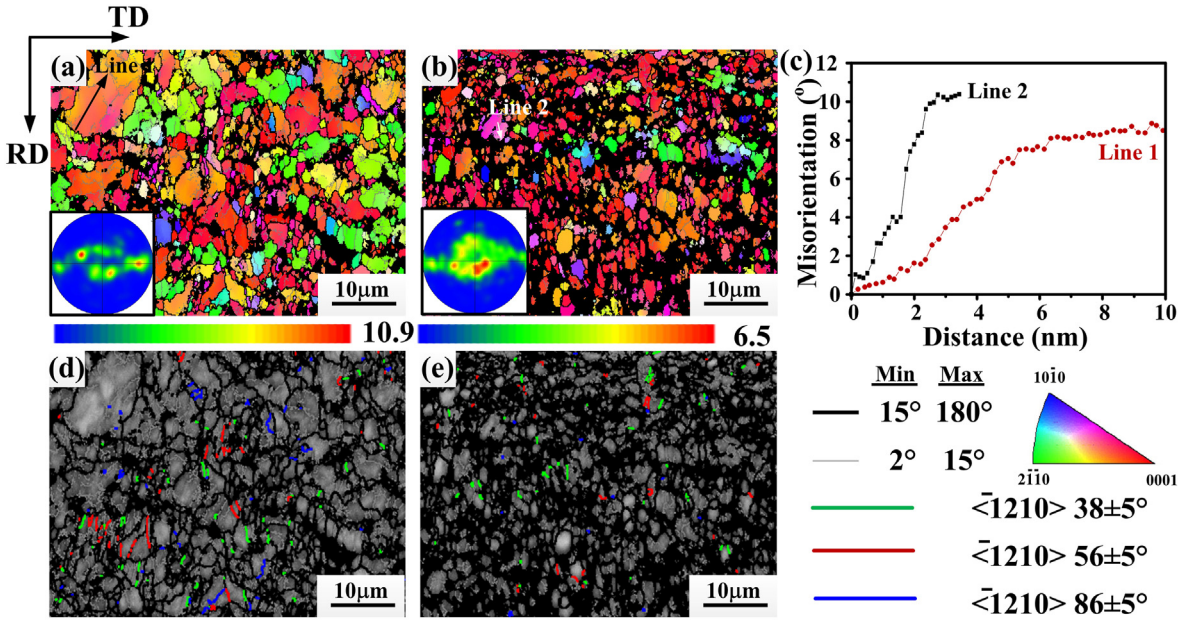

Fig. 3. IPF maps with the corresponding {0001} pole figures for the rolled (a) CS and (b) SRS ZXTM1000 alloys, (c) point to origin misorientation angle profiles along Line 1 and Line 2 in (a) and (b), (d) and (e) band contrast maps superimposed with twin boundaries of the rolled CS and SRS ZXTM1000 alloys, respectively.

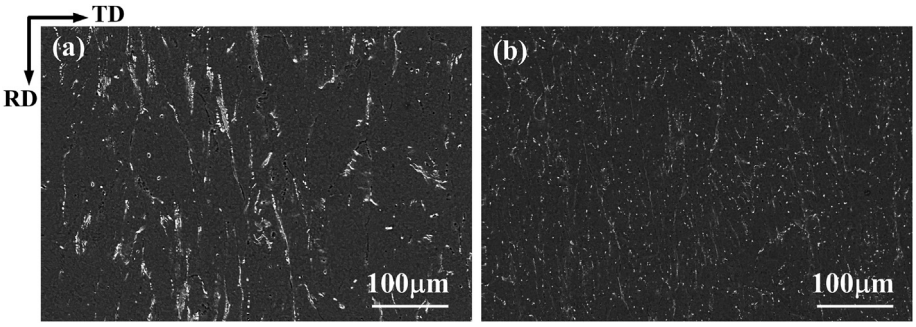

Fig. 4. SEM-BSE micrographs of the rolled and annealed (a) CS and (b) SRS ZXTM1000 alloys.

Zener pinning effect and restricting the grain growth [2,5]. The associated selected area diffraction (SAD) patterns in Fig. 7a, viewing along the zone axis of [$\bar{2}$113], indicates that the A precipitate is $Ca_2Mg_6Zn_3$ phase. Moreover, the corresponding lattice parameters are determined as **a** = 0.983 nm and **c** = 1.018 nm, respectively, which are similar to the reference [36] (**a** = 0.97 nm and **c** = 1.0 nm for $Ca_2Mg_6Zn_3$ precipitate). The nano-sized precipitate B is confirmed to be α-Mn phase based on the high-resolution TEM (HRTEM) image in Fig. 7b. The calculated lattice parameter (**a** = 0.897 nm) for α-Mn shows consistence with the reference [37] (**a** = 0.891 nm). The EDS mapping results (Fig. 7d–g) for the BF-STEM image (Fig. 7c) reveal three types of particles. The nano-sized spherical particles are abundant with Mn, determined as α-Mn phase. Only Ca element is enriched in particles sized in ~100 nm, while the largest spherical particle in the field of view is found to be enriched with Zn and Ca. Consequently, the precipitates in the annealed SRS alloy are expected to be $Ca_2Mg_6Zn_3$, Mg_2Ca, and α-Mn phases.

As shown in Fig. 5f, the annealed SRS ZXTM1000 alloy shows an incompleted recrystallization process, which indicates that there are many substructures, such as residual dislocations, stored within the grains. Further TEM analysis was adopted to reveal the dislocation behaviors, and the results are presented in Fig. 8. Based on the **g**·**b** = 0 invisible criterion [27], the BF-TEM images under the two-beam condition of **g** = [0002] (Fig. 8a and b) show numerous residual dislocations containing <**c**> component. Moreover, under the two-beam condition of **g** = [10$\bar{1}$1] (Fig. 8c and d), there appear more new dislocations (indicated by white arrows) within the grains, determining as <**a**> type dislocations. Previous studies [38,39] showed that basal <**a**> and prismatic <**a**> slips would perform an important role in accommodating the deformation in the Mg–Zn–Ca series alloys. Consequently, the <**a**> dislocations (Fig. 8c and d) in the present study are predicted to include both the basal and prismatic types. The numerous residual dislocations would strengthen the alloy during subsequent tension test, which would be discussed later. The BF-STEM image in Fig. 8e reveals that the dislocations are strongly pinned by α-Mn phases (sized in 10–20 nm) and Ca-containing particles (sized in 100–200 nm). The EDS results (Fig. 8g) of Line 1 in Fig. 8f shows a co-segregation of Zn and Ca atoms at GB.

3.5. Microstructure of the tension-deformed SRS ZXTM1000 alloy

As indicated by the curve of work-hardening rate *vs.* true strain (Fig. 6d), there are multiple slips activated in the tension-deformed SRS ZXTM1000 alloy. EBSD-assisted slip trace analysis, used in

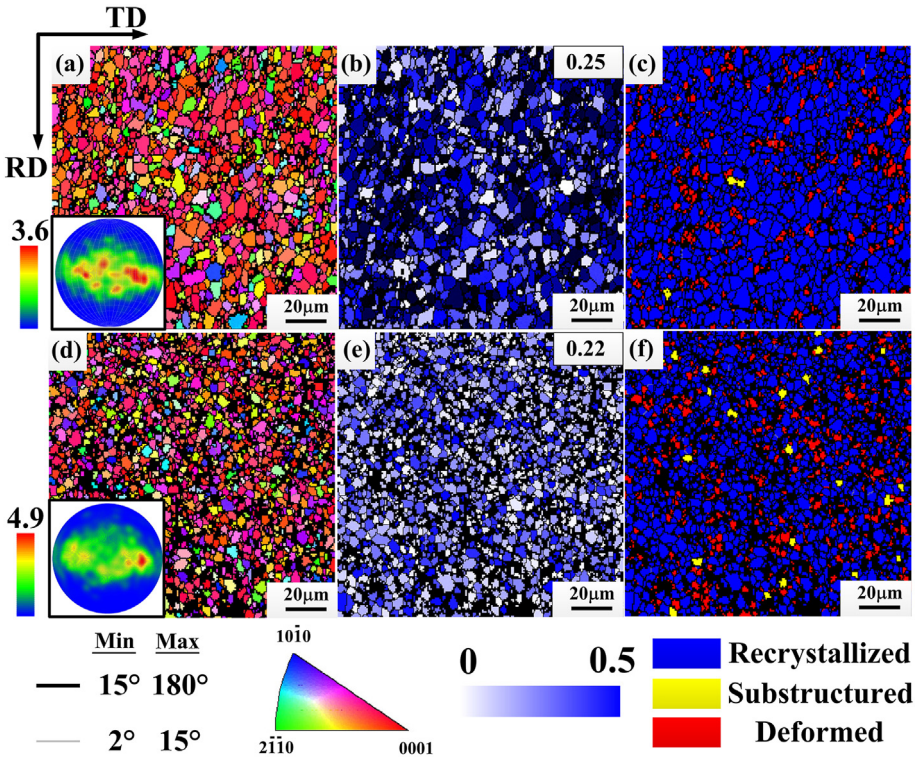

Fig. 5. (a, d) IPF maps with the corresponding {0001} pole figures, (b, e) (0001) <11−20> SF distribution maps, wherein the inserts in (b) and (e) represent the average SF value and (c, f) maps of different types grains for the rolled and annealed (a)−(c) CS and (d)−(f) SRS ZXTM1000 alloys.

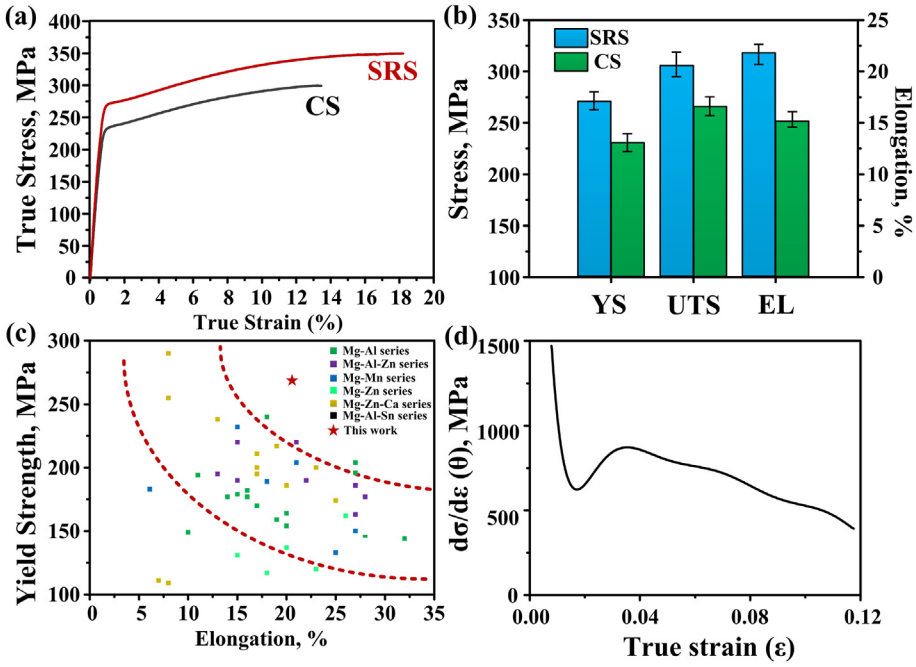

Fig. 6. (a) True stress-strain curves of the annealed CS and SRS ZXTM1000 alloys, (b) comparison of mechanical properties between the annealed CS and SRS ZXTM1000 alloys, (c) yield strength *vs.* elongation for the present annealed SRS ZXTM1000 alloy and other alloys with alloying content <4 wt% [26−35], (d) corresponding work-hardening rate ($d\sigma/d\varepsilon$) *vs.* true strain for the annealed SRS ZXTM1000 alloy.

previous studies [9,40], was utilized to determine the type of slips in the present study. After a ~8% strain, five representative grains with visible slip traces were selected for the SEM examination (Fig. 9a−e), and the corresponding EBSD was obtained for the determination of the grain orientation (Fig. 9f−j). The configuration of an individual slip trace for a specific slip system of the grain was depicted by inputting its Euler angles into a MATLAB code [9,41]. Fig. 9k-o show the results of simulated slip traces, where 1 to 3 represent basal <**a**> slip, 4 to 6 represent prismatic <**a**> slip, and 7 to 12 represent pyramidal II <**c**+**a**> slip. Comparing the experimental slip traces (as

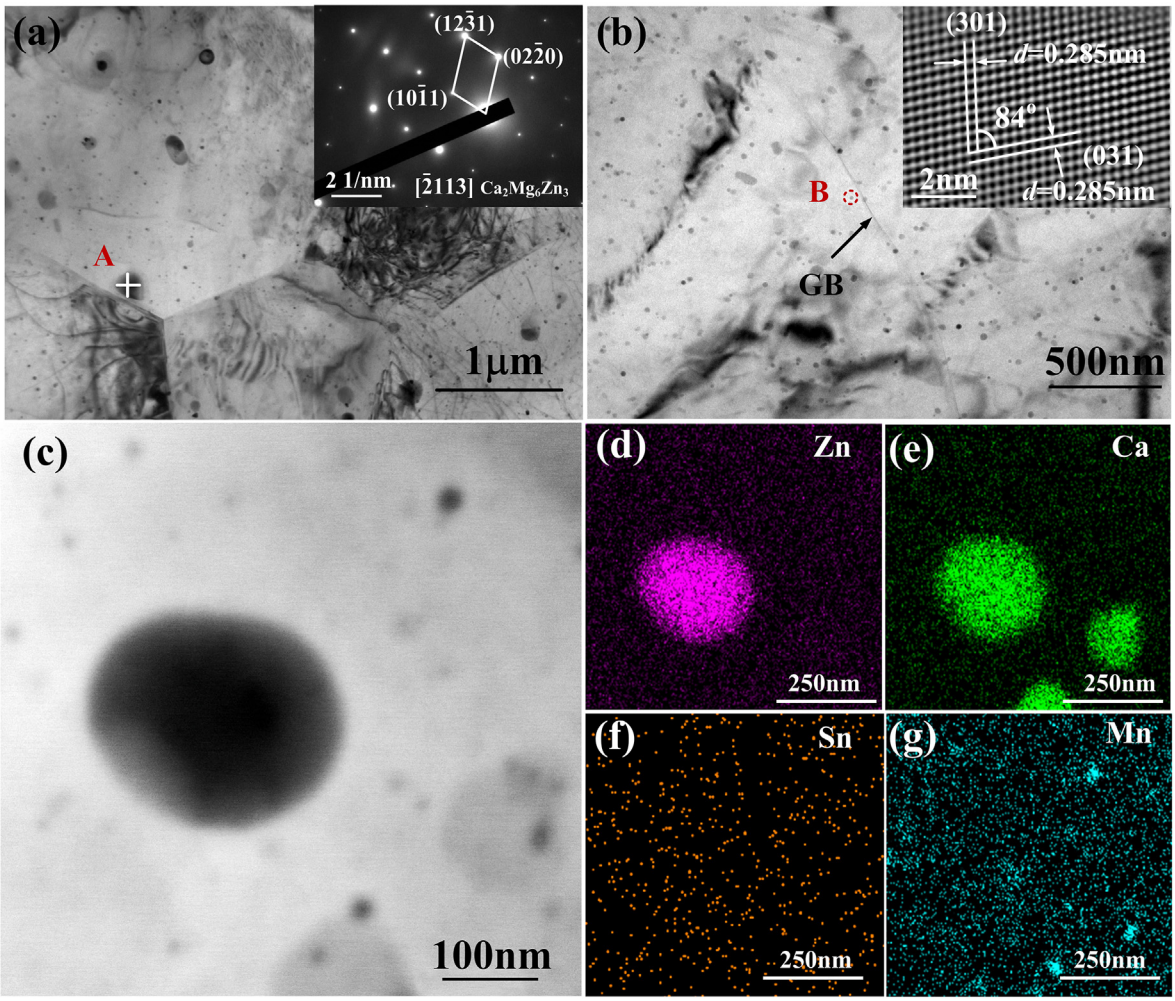

Fig. 7. (a, b) BF-TEM and (c) BF-STEM images of the annealed SRS ZXTM1000 alloy, where the inset in (a) is corresponding SAD patterns for particle A and the inset in (b) is the HRTEM for particle B, (d)–(g) corresponding EDS mapping images of (c).

indicated by the white lines in Fig. 9a–e) with those simulated by the code, the activated slip systems in the five selected grains can be determined as basal <**a**> slip for grains in Fig. 9a and b (as indicated by the red lines in Fig. 9k and l), prismatic <**a**> slip for grains in Fig. 9c and d (as indicated by the red lines in Fig. 9m and n), and pyramidal II <**c**+**a**> slip for grain in Fig. 9e (as indicated by the red line in Fig. 9o). Consequently, it can be concluded that multiple slips, such as basal <**a**> slip, prismatic <**a**> slip and pyramidal II <**c**+**a**> slip, are facilitated during tension test.

4. Discussion

4.1. Microstructure evolution

The annealed SRS ZXTM1000 alloy shows a homogeneous fine-grained (~3 μm) structure (Fig. 5d). As shown in Fig. 7a and b, numerous sub-micron $Ca_2Mg_6Zn_3$, Mg_2Ca, and nano-sized α-Mn are located at GBs, which could suppress the motion of GBs and inhibit the grain growth [2,10]. Besides, there is a considerable co-segregation of Zn and Ca atoms along the GBs (Fig. 8g), triggering the solute dragging force to slow down the migration of GBs and hindering the grain coarsening. Previous study [42] showed that Zn atom with a smaller size than Mg atom tends to segregate to the compression region of dislocation core in GB, whereas Ca atom with a bigger size than Mg atom inclines to diffuse to the extension region, leading to the reduction of GB energy for grain growth.

Moreover, the annealed SRS ZXTM1000 alloy exhibits a TD-split texture, which is different from the intense basal texture of commercial AZ series alloys. After hot rolling, the SRS ZXTM1000 alloy contains many CTWs and DTWs (Fig. 3e), which are considered as the favorable sites to the nucleation of static recrystallized grains with TD-split orientation during subsequent annealing treatment [1]. Besides, the motion of GBs is strongly suppressed by profuse precipitates as well as the enrichment of Zn and Ca atoms at GBs. The Zener pinning effect and solute dragging force would greatly inhibit the preferential growth of the recrystallized grains, and thus resulting in the development of TD-split texture [3,24,42].

4.2. Reasons for high strength – ductility synergy

The microstructure characterization reveals that the main contributing factors for the high YS (~270 MPa) are fine grains, numerous precipitates, and residual dislocations. Note that the annealed SRS ZXTM1000 alloy exhibits a TD-split texture, which would not strengthen the alloy as obvious as the strong basal texture. According to the standard Hall-Petch equation [43]: $\sigma_{grain} = kd^{-1/2}$, where d is the average grain size (~3 μm) and k is the Hall-Petch coefficient (0.313 MPa $m^{0.5}$ for Mg–Zn–Ca series alloys

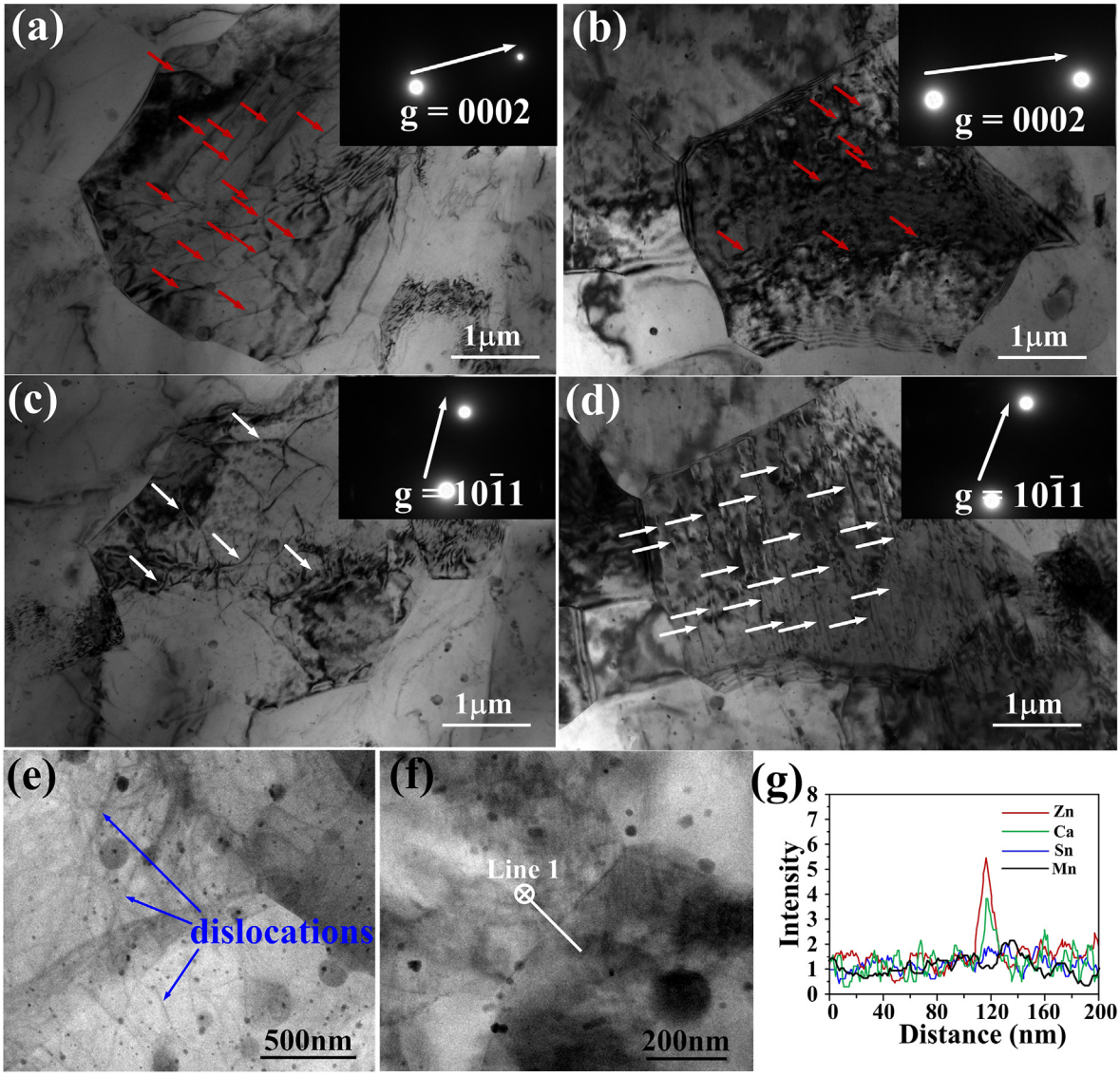

Fig. 8. (a)–(d) BF-TEM images showing dislocation behaviors under the two-beam conditions of (a, b) **g** = [0002], and (c, d) **g** = [10$\bar{1}$1] in two separate grains, (e, f) BF-STEM images, where (e) shows the interaction between precipitates and dislocations; (g) EDS results of Line 1 in (f), showing the co-segregation of Zn and Ca atoms at GB.

[12]), the YS increment from grain refinement is estimated as ~180 MPa, indicating the fine grains strengthening contributes the most to the high YS. Abundant spherical sub-micron and nano-sized second phases are detected within grains (Fig. 7a and b), which would strengthen the alloy via the Orowan strengthening. The Orowan strengthening effect can be predicted by $\sigma_{Orowan} = M\left(\frac{Gb}{2\pi\sqrt{(1-\upsilon)}}\right)\left(\frac{1}{\left(\frac{0.953}{\sqrt{f}}-1\right)D}\right)\left(\log\left(\frac{D}{r_0}\right)\right)$, where M is the average Taylor factor (~2.5 for dominant <**a**> slip), G is the shear modulus (~1.7 × 10^4 MPa), b is the Burgers vector (3.2 × 10^{-10}), υ is the Poisson's ratio (~0.3), D is the mean particle diameter (~160 nm for Ca-containing precipitates and ~15 nm for α-Mn particles), f is the volume fraction of precipitates (~3.5% for Ca-containing precipitates and ~0.7% for α-Mn particles) and r_0 is the dislocation core radius (0.32 nm) [43]. At least 5 images were used to calculate the volume fraction of the particles. For simplicity, the whole Orowan strengthening is the linear superposition of the two types of second phases. Accordingly, the calculated value of precipitation hardening in the annealed SRS ZXTM1000 alloy is ~39 MPa.

Furthermore, as revealed in Fig. 8, numerous dislocations are retained after annealing, which can improve the YS of the annealed SRS ZXTM1000 alloy based on the Taylor law [44]. The increment of YS induced by residual dislocations is dependent on the dislocation density, calculated by $\rho = 2\theta/ub$, where ρ is the GND density, θ represents the local misorientation (<3°), b is the Burgers vector (0.32 nm for Mg), and u is the unit length (step size, 600 nm) [44]. The calculated dislocation density is 6.0 × 10^{13} m^{-2}, and thus the increment of YS related to dislocation strengthening can be calculated by: $\sigma_{dis} = \alpha MGb\sqrt{\rho}$, where α is a constant (0.2), M is the average Taylor factor, G is the shear modulus, b is the Burgers vector [44]. The contribution of residual dislocations to strengthening is estimated as ~21 MPa. By summing the contributions from the fine-grain strengthening, precipitation strengthening, dislocation strengthening, and friction stress (σ_0) for pure Mg (25 MPa), the predicted YS of the annealed SRS ZXTM1000 alloy is ~265 MPa. There is a minor gap between the predicted YS and the experimental value (~270 MPa), which may be originated from the solid-solution strengthening.

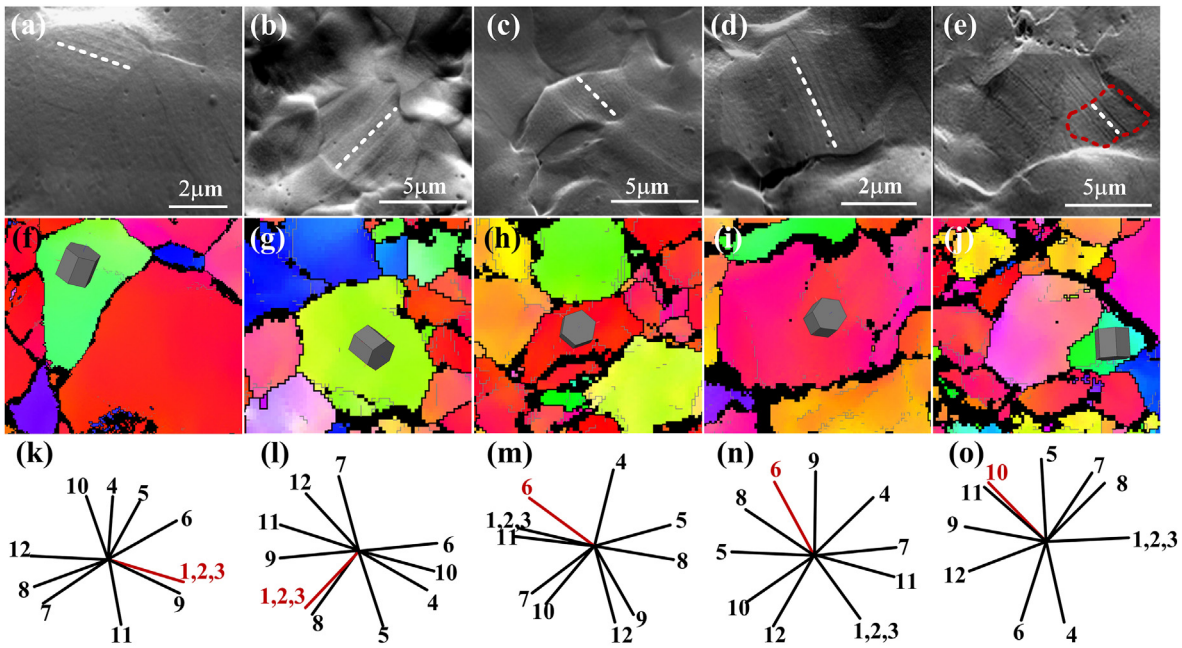

Fig. 9. (a)–(e) SEM images illustrating the traces (indicated by the white dot lines), (f)–(j) corresponding IPF maps showing the orientation of the selected grains, (k)–(o) the calculation of the 12 possible traces for the selected grains obtained from the annealed SRS ZXTM1000 alloy after a strain of ~8%. (1–3 represent basal <**a**> slips, 4 to 6 represent prismatic <**a**> slips, and 7 to 12 represent pyramidal II <**c**+**a**> slips).

In general, good ductility usually means that more uniform deformation occurs and more slip modes are activated during deformation. A homogeneous fine-grained (~3 μm) structure with TD-split texture can enhance dislocation storage, and therefore delaying the occurrence of necking and improving the ductility [38]. It is accepted that an enhanced work-hardening rate implies an improved resistance to plasticity instability. The high density of precipitates within grains (Fig. 7a and b) would be beneficial to improve the work-hardening rate by inhibiting the dynamic recovery of dislocations, and thus ameliorating the ductility [44,45].

Moreover, the introduction of Zn and Ca atoms in the Mg matrix would also affect the critical resolved shear stress (CRSS) of basal and non-basal slip systems, and accordingly influence the ductility of the alloys. Blake et al. [46] reported that the moderate increment of ductility in Mg–Zn alloys originates from the softening of prismatic <**a**> slip due to the addition of Zn element. Previous studies [3,11,40,47] also reported that the co-addition of Zn and Ca reduces the difference in the CRSS of prismatic <**a**> with respect to basal <**a**> slip, leading to enhanced prismatic slips to accommodate deformation and therefore improved ductility. Furthermore, the solid-solution of Zn and Ca atoms in the Mg matrix contribute to the decrease of I_1SFE [48], which may be beneficial for the operation of <**c**+**a**> slips to accommodate deformation in the present study. Therefore, the good ductility in the present annealed SRS ZXTM1000 alloy can be guaranteed by the homogeneous fine-grained structure, enhanced work-hardening rate, and the activation of multiple types of slips.

5. Conclusion

To summarize, a new wrought ZXTM1000 alloy sheet, exhibiting an excellent combination of YS (~270 MPa) and elongation (~21%), was fabricated by the SRS, hot-rolling, and annealing. The SRS obviously refines the eutectic CaMgSn and $Ca_2Mg_6Zn_3$ phases, which is beneficial to the microstructure homogenization and grain refinement, leading to the YS increment of ~45 MPa, UTS increment of ~50 MPa, and EL increment of ~7% than that of the CS counterpart. The annealed SRS ZXTM1000 alloy shows a fine-grained structure (~3 μm) which is stabilized by profuse nanoscale (10–200 nm) spherical $Ca_2Mg_6Zn_3$, Mg_2Ca, and α-Mn precipitates, and the co-segregation of Zn and Ca atoms at GBs. Moreover, the annealed SRS ZXTM1000 alloy contains a high density of residual dislocations, which play as a contributing factor for the achievement of high strength. Fine-grains strengthening and precipitate strengthening are considered to be the main reasons for the high YS, while the improved ductility is attributed to the uniform grain size distribution, enhanced work-hardening capacity, and the activation of multiple types of slips. Therefore, the present study provides an effective way to fabricate low-alloyed Mg alloys with simultaneously enhanced strength and ductility by coupling the SRS and hot rolling.

CRediT authorship contribution statement

Zhen-Ming Hua: conceived and designed the initial idea, performed the experiments, wrote the article manuscript, analyzed and interpreted the experimental data, collected and assembled data. **Bing-Yu Wang:** performed the experiments, analyzed and interpreted the experimental data, collected and assembled data. **Cheng Wang:** conceived and designed the initial idea, analyzed and interpreted the experimental data, revised the manuscript for publication. **Chen-Yi Ma:** performed the experiments, analyzed and interpreted the experimental data, collected and assembled data. **Pin-Kui Ma:** analyzed and interpreted the experimental data. **Zhi-Ping Guan:** analyzed and interpreted the experimental data. **Yi-Jia Li:** performed the experiments, collected and assembled data. **Jia-Sheng Li:** performed the experiments, collected and assembled data. **Hui-Yuan Wang:** conceived and designed the initial idea, revised the manuscript for publication.

Declaration of competing interest

The authors declare that they have no known competing financial interests or personal relationships that could have appeared to influence the work reported in this paper.

Acknowledgment

Financial supports from The National Natural Science Foundation of China (Nos. 51625402, U19A2084, 51790483, and 51801069) are greatly acknowledged. Partial financial support came from The Science and Technology Development Program of Jilin Province (Nos. 20200401025GX and 20200201002JC), Program for JLU Science and Technology Innovative Research Team (JLUSTIRT, 2017TD-09), and The Changjiang Scholars Program (T2017035).

References

[1] Z.H. Li, T.T. Sasaki, M.Z. Bian, T. Nakata, Y. Yoshida, N. Kawabe, S. Kamado, K. Hono, Role of Zn on the room temperature formability and strength in Mg–Al–Ca–Mn sheet alloys, J. Alloys Compd. 847 (2020) 156347, https://doi.org/10.1016/j.jallcom.2020.156347.

[2] X. Chen, D. Zhang, J. Xu, J. Feng, Y. Zhao, B. Jiang, F. Pan, Improvement of mechanical properties of hot extruded and age treated Mg–Zn–Mn–Ca alloy through Sn addition, J. Alloys Compd. (2020) 156711, https://doi.org/10.1016/j.jallcom.2020.156711.

[3] L.-Q. Zhao, C. Wang, J.-C. Chen, H. Ning, Z.-Z. Yang, J. Xu, H.-Y. Wang, Development of weak-textured and high-performance Mg–Zn–Ca alloy sheets based on Zn content optimization, J. Alloys Compd. 849 (2020) 156640, https://doi.org/10.1016/j.jallcom.2020.156640.

[4] T.T. Sasaki, F.R. Elsayed, T. Nakata, T. Ohkubo, S. Kamado, K. Hono, Strong and ductile heat-treatable Mg–Sn–Zn–Al wrought alloys, Acta Mater. 99 (2015) 176–186, https://doi.org/10.1016/j.actamat.2015.06.060.

[5] X. Liu, X. Qiao, Z. Li, M. Zheng, High strength and excellent ductility of dilute Mg-0.68Al-0.32Ca-0.50Mn (wt%) extrusion alloy obtained by T6 treatment, Mater. Char. 162 (2020) 110197, https://doi.org/10.1016/j.matchar.2020.110197.

[6] H.-M. Zhang, X.-M. Cheng, M. Zha, Y.-K. Li, C. Wang, Z.-Z. Yang, J.-G. Wang, H.-Y. Wang, A superplastic bimodal grain-structured Mg–9Al–1Zn alloy processed by short-process hard-plate rolling, Materialia 8 (2019) 100443, https://doi.org/10.1016/j.mtla.2019.100443.

[7] C. Wang, A. Ma, J. Sun, H. Liu, H. Huang, Z. Yang, J. Jiang, Effect of ECAP process on as-cast and as-homogenized Mg-Al-Ca-Mn alloys with different Mg_2Ca morphologies, J. Alloys Compd. 793 (2019) 259–270, https://doi.org/10.1016/j.jallcom.2019.04.202.

[8] J. Suh, J. Victoria-Hernández, D. Letzig, R. Golle, W. Volk, Effect of processing route on texture and cold formability of AZ31 Mg alloy sheets processed by ECAP, Mater. Sci. Eng., A 669 (2016) 159–170, https://doi.org/10.1016/j.msea.2016.05.027.

[9] C.M. Cepeda-Jiménez, M. Castillo-Rodríguez, M.T. Pérez-Prado, Origin of the low precipitation hardening in magnesium alloys, Acta Mater. 165 (2019) 164–176, https://doi.org/10.1016/j.actamat.2018.11.044.

[10] L.B. Tong, J.H. Chu, W.T. Sun, Z.H. Jiang, D.N. Zou, K.S. Wang, S. Kamado, M.Y. Zheng, Development of high-performance Mg–Zn–Ca–Mn alloy via an extrusion process at relatively low temperature, J. Alloys Compd. 825 (2020) 153942, https://doi.org/10.1016/j.jallcom.2020.153942.

[11] G. Zhu, L. Wang, H. Zhou, J. Wang, Y. Shen, P. Tu, H. Zhu, W. Liu, P. Jin, X. Zeng, Improving ductility of a Mg alloy via non-basal <a> slip induced by Ca addition, Int. J. Plast. 120 (2019) 164–179, https://doi.org/10.1016/j.ijplas.2019.04.020.

[12] C.-j. Li, H.-f. Sun, X.-w. Li, J.-l. Zhang, W.-b. Fang, Z.-y. Tan, Microstructure, texture and mechanical properties of Mg-3.0Zn-0.2Ca alloys fabricated by extrusion at various temperatures, J. Alloys Compd. 652 (2015) 122–131, https://doi.org/10.1016/j.jallcom.2015.08.215.

[13] Y. Chai, B. Jiang, J. Song, Q. Wang, H. Gao, B. Liu, G. Huang, D. Zhang, F. Pan, Improvement of mechanical properties and reduction of yield asymmetry of extruded Mg-Sn-Zn alloy through Ca addition, J. Alloys Compd. 782 (2019) 1076–1086, https://doi.org/10.1016/j.jallcom.2018.12.109.

[14] Z.T. Li, X.G. Qiao, C. Xu, X.Q. Liu, S. Kamado, M.Y. Zheng, Enhanced strength by precipitate modification in wrought Mg–Al–Ca alloy with trace Mn addition, J. Alloys Compd. 836 (2020) 154689, https://doi.org/10.1016/j.jallcom.2020.154689.

[15] W. Li, X. Huang, W. Huang, Effects of Ca, Ag addition on the microstructure and age-hardening behavior of a Mg-7Sn (wt%) alloy, Mater. Sci. Eng., A 692 (2017) 75–80, https://doi.org/10.1016/j.msea.2017.03.066.

[16] X. Lu, G. Zhao, J. Zhou, C. Zhang, J. Yu, Microstructure and mechanical properties of the as-cast and as-homogenized Mg-Zn-Sn-Mn-Ca alloy fabricated by semicontinuous casting, Materials 11 (2018) 11–31, https://doi.org/10.3390/ma11050703.

[17] S.W. Xu, K. Oh-ishi, S. Kamado, H. Takahashi, T. Homma, Effects of different cooling rates during two casting processes on the microstructures and mechanical properties of extruded Mg–Al–Ca–Mn alloy, Mater. Sci. Eng., A 542 (2012) 71–78, https://doi.org/10.1016/j.msea.2012.02.034.

[18] Z.-T. Liu, B.-Y. Wang, C. Wang, M. Zha, G.-J. Liu, Z.-Z. Yang, J.-G. Wang, J.-H. Li, H.-Y. Wang, Microstructure and mechanical properties of Al-Mg-Si alloy fabricated by a short process based on sub-rapid solidification, J. Mater. Sci. Technol. 41 (2020) 178–186, https://doi.org/10.1016/j.jmst.2019.08.053.

[19] C.-Y. Ma, C. Wang, Z.-M. Hua, P.-Y. Wang, J.-G. Wang, H.-Y. Wang, A high-performance Mg-Al-Sn-Zn-Bi alloy fabricated by combining sub-rapid solidification and hot rolling, Mater. Char. 169 (2020) 110580, https://doi.org/10.1016/j.matchar.2020.110580.

[20] Z.T. Liu, C. Wang, Q. Luo, J. You, X.L. Zhou, J. Xu, Y.T. Mo, J.W. Song, M. Zha, H.Y. Wang, Effects of Mg contents on the microstructure evolution and Fe–bearing phase selection of Al–Mg–Si–Fe alloys under sub–rapid solidification, Materialia 13 (2020) 100850, https://doi.org/10.1016/j.mtla.2020.100850.

[21] F. Wang, R. Zheng, J. Chen, S. Lyu, Y. Li, W. Xiao, C. Ma, Significant improvement in the strength of Mg-Al-Zn-Ca-Mn extruded alloy by tailoring the initial microstructure, Vacuum 161 (2019) 429–433, https://doi.org/10.1016/j.vacuum.2019.01.016.

[22] Q. Du, Y. Li, An extension of the Kampmann–Wagner numerical model towards as-cast grain size prediction of multicomponent aluminum alloys, Acta Mater. 71 (2014) 380–389, https://doi.org/10.1016/j.actamat.2014.03.028.

[23] K. Huang, R.E. Logé, A review of dynamic recrystallization phenomena in metallic materials, Mater. Des. 111 (2016) 548–574, https://doi.org/10.1016/j.matdes.2016.09.012.

[24] D. Guan, W.M. Rainforth, J. Gao, J. Sharp, B. Wynne, L. Ma, Individual effect of recrystallisation nucleation sites on texture weakening in a magnesium alloy: Part 1- double twins, Acta Mater. 135 (2017) 14–24, https://doi.org/10.1016/j.actamat.2017.06.015.

[25] S.M. Baek, H.K. Park, J.I. Yoon, J. Jung, J.H. Moon, S.G. Lee, J.H. Kim, T.S. Kim, S. Lee, N.J. Kim, H.S. Kim, Effect of secondary phase particles on the tensile behavior of Mg-Zn-Ca alloy, Mater. Sci. Eng., A 735 (2018) 288–294, https://doi.org/10.1016/j.msea.2018.08.050.

[26] M.Z. Bian, T.T. Sasaki, B.C. Suh, T. Nakata, S. Kamado, K. Hono, A heat-treatable Mg–Al–Ca–Mn–Zn sheet alloy with good room temperature formability, Scripta Mater. 138 (2017) 151–155, https://doi.org/10.1016/j.scriptamat.2017.05.034.

[27] M.Z. Bian, T.T. Sasaki, T. Nakata, Y. Yoshida, N. Kawabe, S. Kamado, K. Hono, Bake-hardenable Mg–Al–Zn–Mn–Ca sheet alloy processed by twin-roll casting, Acta Mater. 158 (2018) 278–288, https://doi.org/10.1016/j.actamat.2018.07.057.

[28] M. Yuasa, N. Miyazawa, M. Hayashi, M. Mabuchi, Y. Chino, Effects of group II elements on the cold stretch formability of Mg–Zn alloys, Acta Mater. 83 (2015) 294–303, https://doi.org/10.1016/j.actamat.2014.10.005.

[29] G. Wang, G. Huang, X. Chen, Q. Deng, A. Tang, B. Jiang, F. Pan, Effects of Zn addition on the mechanical properties and texture of extruded Mg-Zn-Ca-Ce magnesium alloy sheets, Mater. Sci. Eng., A 705 (2017) 46–54, https://doi.org/10.1016/j.msea.2017.08.036.

[30] B.P. Zhang, L. Geng, L.J. Huang, X.X. Zhang, C.C. Dong, Enhanced mechanical properties in fine-grained Mg–1.0Zn–0.5Ca alloys prepared by extrusion at different temperatures, Scripta Mater. 63 (2010) 1024–1027, https://doi.org/10.1016/j.scriptamat.2010.07.038.

[31] X. Huang, K. Suzuki, Y. Chino, M. Mabuchi, Influence of aluminum content on the texture and sheet formability of AM series magnesium alloys, Mater. Sci. Eng., A 633 (2015) 144–153, https://doi.org/10.1016/j.msea.2015.03.018.

[32] J. She, F. Pan, J. Zhang, A. Tang, S. Luo, Z. Yu, K. Song, M. Rashad, Microstructure and mechanical properties of Mg–Al–Sn extruded alloys, J. Alloys Compd. 657 (2016) 893–905, https://doi.org/10.1016/j.jallcom.2015.10.146.

[33] Q. Li, G.J. Huang, X.D. Huang, S.W. Pan, C.L. Tan, Q. Liu, On the texture evolution of Mg–Zn–Ca alloy with different hot rolling paths, J. Magnes. alloys 5 (2017) 166–172, https://doi.org/10.1016/j.jma.2017.06.001.

[34] J. Victoria-Hernández, S. Yi, D. Klaumünzer, D. Letzig, Recrystallization behavior and its relationship with deformation mechanisms of a hot rolled Mg-Zn-Ca-Zr alloy, Mater. Sci. Eng., A 761 (2019) 138054, https://doi.org/10.1016/j.msea.2019.138054.

[35] T. Nakata, C. Xu, R. Ajima, K. Shimizu, S. Hanaki, T.T. Sasaki, L. Ma, K. Hono, S. Kamado, Strong and ductile age-hardening Mg-Al-Ca-Mn alloy that can be extruded as fast as aluminum alloys, Acta Mater. 130 (2017) 261–270, https://doi.org/10.1016/j.actamat.2017.03.046.

[36] K. Oh-ishi, R. Watanabe, C.L. Mendis, K. Hono, Age-hardening response of Mg–0.3at.%Ca alloys with different Zn contents, Mater. Sci. Eng., A 526 (2009) 177–184, https://doi.org/10.1016/j.msea.2009.07.027.

[37] P. Duley, S. Sanyal, T.K. Bandyopadhyay, S. Mandal, Implications of grain size distribution, precipitate evolution and texture development on tensile properties in hard plate hot forged and annealed Mg–Zn–Ca–Mn alloy, Mater. Sci. Eng., A 784 (2020) 139288, https://doi.org/10.1016/j.msea.2020.139288.

[38] Z.R. Zeng, M.Z. Bian, S.W. Xu, C.H.J. Davies, N. Birbilis, J.F. Nie, Effects of dilute additions of Zn and Ca on ductility of magnesium alloy sheet, Mater. Sci. Eng., A 674 (2016) 459–471, https://doi.org/10.1016/j.msea.2016.07.049.

[39] C. Ha, J. Bohlen, S. Yi, X. Zhou, H.-G. Brokmeier, N. Schell, D. Letzig, K.U. Kainer, Influence of Nd or Ca addition on the dislocation activity and texture changes of Mg–Zn alloy sheets under uniaxial tensile loading, Mater. Sci. Eng., A 761 (2019) 138053, https://doi.org/10.1016/j.msea.2019.138053.

[40] D.F. Shi, M.T. Pérez-Prado, C.M. Cepeda-Jiménez, Effect of solutes on strength and ductility of Mg alloys, Acta Mater. 180 (2019) 218–230, https://doi.org/10.1016/j.actamat.2019.09.018.

[41] C.M. Cepeda-Jiménez, J.M. Molina-Aldareguia, M.T. Pérez-Prado, Effect of grain size on slip activity in pure magnesium polycrystals, Acta Mater. 84 (2015) 443–456, https://doi.org/10.1016/j.actamat.2014.10.001.

[42] Z.R. Zeng, Y.M. Zhu, S.W. Xu, M.Z. Bian, C.H.J. Davies, N. Birbilis, J.F. Nie, Texture evolution during static recrystallization of cold-rolled magnesium

alloys, Acta Mater. 105 (2016) 479–494, https://doi.org/10.1016/j.actamat.2015.12.045.
[43] Y.-h. Liu, W.-l. Cheng, Y. Zhang, X.-f. Niu, H.-x. Wang, L.-f. Wang, Microstructure, tensile properties, and corrosion resistance of extruded Mg-1Bi-1Zn alloy: the influence of minor Ca addition, J. Alloys Compd. 815 (2020) 152414, https://doi.org/10.1016/j.jallcom.2019.152414.
[44] H. Pan, R. Kang, J. Li, H. Xie, Z. Zeng, Q. Huang, C. Yang, Y. Ren, G. Qin, Mechanistic investigation of a low-alloy Mg–Ca-based extrusion alloy with high strength–ductility synergy, Acta Mater. 186 (2020) 278–290, https://doi.org/10.1016/j.actamat.2020.01.017.
[45] W.Z. Chen, X. Wang, E.D. Wang, Z.Y. Liu, L.X. Hu, Texture dependence of uniform elongation for a magnesium alloy, Scripta Mater. 67 (2012) 858–861, https://doi.org/10.1016/j.scriptamat.2012.08.009.
[46] A.H. Blake, C.H. Cáceres, Solid-solution hardening and softening in Mg–Zn alloys, Mater. Sci. Eng., A 483–484 (2008) 161–163, https://doi.org/10.1016/j.msea.2006.10.205.
[47] C. Zhao, X. Chen, F. Pan, J. Wang, S. Gao, T. Tu, C. Liu, J. Yao, A. Atrens, Strain hardening of as-extruded Mg-xZn (x = 1, 2, 3 and 4 wt%) alloys, J. Mater. Sci. Technol. 35 (2019) 142–150, https://doi.org/10.1016/j.jmst.2018.09.015.
[48] S. Meng, H. Yu, L. Li, J. Qin, S.K. Woo, Y. Go, Y.M. Kim, S.H. Park, W. Zhao, F. Yin, B.S. You, K.S. Shin, Effects of Ca addition on the microstructures and mechanical properties of as-extruded Mg–Bi alloys, J. Alloys Compd. 834 (2020) 155216, https://doi.org/10.1016/j.jallcom.2020.155216.